

Temperature-Controlled Synthesis of Li- and Mn-Rich $\text{Li}_{1.2}\text{Mn}_{0.54}\text{Ni}_{0.13}\text{Co}_{0.13}\text{O}_2$ Hollow Nano/Sub-Microsphere Electrodes for High-Performance Lithium-Ion Battery

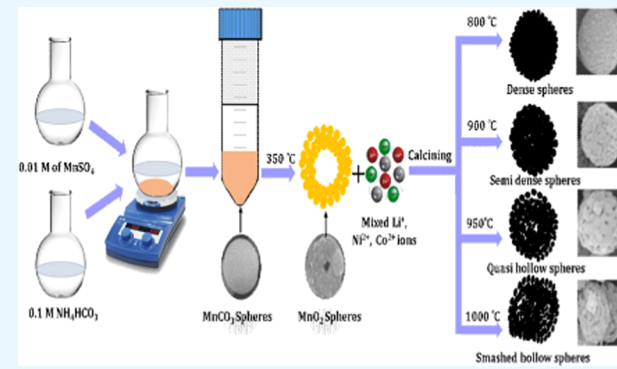
Srinivasan Alagar,[†] Chelladurai Karuppiah,[‡] Rajesh Madhuviakku,[†] Shakkthivel Piraman,^{*,†} and Chun-Chen Yang^{*,‡}

[†]Sustainable Energy and Smart Materials Research Lab, Department of Nanoscience and Technology, Science Campus, Alagappa University, Karaikudi 630002, Tamil Nadu, India

[‡]Battery Research Center of Green Energy, Ming Chi University of Technology, New Taipei City 24301, Taiwan, ROC

Supporting Information

ABSTRACT: The calcination temperature plays a significant role in the structural, textural, and energy-storage performance of metal oxide nanomaterials in Li-ion battery application. Here, we report the formation of well-crystallized homogeneously dispersed $\text{Li}_{1.2}\text{Mn}_{0.54}\text{Ni}_{0.13}\text{Co}_{0.13}\text{O}_2$ hollow nano/sub-microsphere architectures through a simple cost-effective coprecipitation and chemical mixing route without surface modification for improving the efficiency of energy storage devices. The synthesized $\text{Li}_{1.2}\text{Mn}_{0.54}\text{Ni}_{0.13}\text{Co}_{0.13}\text{O}_2$ hollow nano/sub-microsphere cathode materials are calcined at 800, 900, 950, and 1000 °C. Among them, $\text{Li}_{1.2}\text{Mn}_{0.54}\text{Ni}_{0.13}\text{Co}_{0.13}\text{O}_2$ calcined at 950 °C exhibits a high discharge capacity (277 mAh g⁻¹ at 0.1C rate) and excellent capacity retention (88%) after 50 cycles and also delivers an excellent discharge capacity of >172 mAh g⁻¹ at 5C rate. Good electrochemical performance of $\text{Li}_{1.2}\text{Mn}_{0.54}\text{Ni}_{0.13}\text{Co}_{0.13}\text{O}_2$ -950 is directly related to the optimized size of its primary particles (85 nm) (which constitute the spherical secondary particle, ~720 nm) and homogeneous cation mixing. Higher calcination temperature (≥950 °C) leads to an increase of the primary particle size, poor cycling stability, and inferior rate capacity of $\text{Li}_{1.2}\text{Mn}_{0.54}\text{Ni}_{0.13}\text{Co}_{0.13}\text{O}_2$ due to smashing of quasi-hollow spheres upon repeated lithium ion intercalations/deintercalations. Therefore, $\text{Li}_{1.2}\text{Mn}_{0.54}\text{Ni}_{0.13}\text{Co}_{0.13}\text{O}_2$ -950 is a promising electrode for the next-generation high-voltage and high-capacity Li-ion battery application.



1. INTRODUCTION

The drastic production of greenhouse gases resulting from the widespread use of fossil fuels has been attracting considerable attention worldwide. To solve these problems, alternative energy resources and/or the robust energy storage systems are crucially needed in the current stage. Lithium-ion batteries (LIBs) have found a prominent place in the energy storage systems, particularly in the electric vehicles, hybrid electric vehicles, and large-scale grid-based electrical energy storage systems.^{1–3} However, the commercially available cathode materials, such as layered (LiCoO_2 , $\text{LiNi}_{1/3}\text{Mn}_{1/3}\text{Co}_{1/3}\text{O}_2$), spinel (LiMn_2O_4 , $\text{LiNi}_{0.5}\text{Mn}_{1.5}\text{O}_4$), and olivine (LiFePO_4), cannot fully satisfy the current demands such as high energy density and low cost. In this direction, Li-rich layered oxides Li_2MnO_3 – LiMO_2 (M = Co, Ni, and Mn) are promising cathode materials, owing to their high capacity, enhanced cyclic stability, and low cost.^{4–8} The high voltage plateau (4.5 V) of LiMn_2O_3 and Li_xMnO_2 formation along the electrochemical phenomenon is attributed to the activation of LiMn_2O_3 , which is responsible for its excellent discharge capacity above 250 mAh g⁻¹.^{9,10} However, some disadvantages

still need to be overcome before the practical applications in LIBs such as tap density, low initial Columbic efficiency, poor high-rate performance, and cycling capacity fading.¹¹

To date, significant effort has been dedicated to improve the electrochemical performance of the Li- and Mn-rich layered cathode materials by surface modification,^{12,13} lattice doping,¹⁴ and tuning the material composition.¹⁵ Moreover, the synthetic conditions, such as coprecipitation,^{16,17} lithium content,^{18,19} particle size,²⁰ calcination temperature,²¹ calcination atmosphere (O₂, air, etc.), and heating and cooling rates^{22,23} are also varied to examine the electrochemical performance of Li- and Mn-rich layered cathode materials. Furthermore, it has been confirmed that some electrode materials based on nano/sub-micro architecture morphologies, such as nanoplates²⁴ and nanosheets,²⁵ are greatly helpful to the enhancement of high-rate capabilities of Li-ion cathode materials. In addition, hollow or porous microparticles of

Received: August 27, 2019

Accepted: October 18, 2019

Published: November 21, 2019

cathode materials have been reported for the improvement of electrochemical performance.^{26,27} The cavities present in the hollow microparticles could provide more active sites for Li⁺ ion storage, which is beneficial for increasing the reversible capacity. In this microstructure, the secondary hollow nano/sub-micron-sized particles consist of nanosized primary particles and possess a larger surface area. The larger surface area and mesoporous nature of the electrodes provide more Li ion diffusion access to the electrolyte, attributed to the improvement of high-rate capability. Finally, the void space in the hollow nano/sub-microsphere particles could offer an extra space for volume expansion/contraction in the process of Li⁺ intercalations/deintercalations, which could facilitate the improvement of electrochemical performances.^{28–32}

Considering the advantage of cost-effective and simplified preparation, the coprecipitation route would be of great interest. The coprecipitation method is applicable for the direct control of the particle nano/sub-microstructure, size, and shape. In this work, we demonstrated the $\text{Li}_{1.2}\text{Mn}_{0.54}\text{Ni}_{0.13}\text{Co}_{0.13}\text{O}_2$ (LMNCO) hollow nano/sub-microsphere preparation using a MnO_2 hollow nanosphere template. The effect of calcination temperature on the primary nanoparticle size, cation mixing, and electrochemical performance of a Li- and Mn-rich cathode material Li-ion cell (LMNCO), with a large secondary particle size, required for reaching a high volumetric density, is evaluated. The Li-ion cell with LMNCO material calcined at different temperatures (800–1000 °C) was cycled with a high cutoff voltage of 4.8 V; LMNCO-950 showed significantly improved performance and thus the Li- and Mn-rich cathode materials can be adopted for high-capacity and high-voltage LIB applications.

2. RESULTS AND DISCUSSION

2.1. Material Characterization. Figure S1 displays the scanning electron microscopy (SEM) images of MnCO_3 nanospheres (a and b) and MnO_2 hollow nano/sub-microspheres (c and d) at different magnifications. Legibly, MnCO_3 solid spheres prepared by the coprecipitation method are seen (400–550 nm) and employed as a self-template, and MnCO_3 nanospheres are converted into MnO_2 hollow spheres by thermal decomposition at 350 °C. The $\alpha\text{-MnO}_2$ hollow nano/sub-microsphere template precursors show relatively uniform sizes, about 400–600 nm, with a hollow nano/sub-microsphere morphology. We observed the hollow morphology of secondary particles; according to the Kirkendall effect, during the calcination process, the metal atoms rapidly diffuse outward and the opposite O atom slowly diffuse inward, which leads to the formation of the hollow MnO_2 precursor; moreover, the CO_3^{2-} ion decomposition is also involved in the hollow structure formation process. The thermal decomposition of the MnO_2 hollow nano/sub-microsphere precursor with Ni, Co, and Li source salts and the formation of $\text{Li}_{1.2}\text{Mn}_{0.54}\text{Co}_{0.13}\text{Ni}_{0.13}\text{O}_2$ (LMNCO) hollow nano/sub-microspheres were measured by thermogravimetric analysis/differential thermal analysis (TGA/DTA) and are presented in Figure S2. There were three major weight losses found in the temperature range from 25 to 1000 °C. The first weight loss was measured to be 7% (25–180 °C), which can be attributed to the loss of hygroscopic nature and coordination-bonded water molecules. The second drastic weight loss from 180 to 400 °C was ascribed to the thermal decomposition of nitrates of Ni, Co, and LiOH along with interstitial H_2O . The third weight loss region at 350–652 °C may be due to the complete

elimination of organic moieties and unwanted gaseous matter along with structural re-orientation. The reaction between transition metal oxides and Li salts occurs below 800 °C, and the formation of a Li-rich structure is accomplished above 800 °C.^{7,33} Finally, there was no considerable weight loss found beyond 800 °C temperature, and it can be interpreted that the $\text{Li}_{1.2}\text{Mn}_{0.54}\text{Co}_{0.13}\text{Ni}_{0.13}\text{O}_2$ hollow nano/sub-microsphere samples were stable at a higher temperature. Hence, the effect of various calcination temperatures on the electrochemical performances was evaluated using the $\text{Li}_{1.2}\text{Mn}_{0.54}\text{Co}_{0.13}\text{Ni}_{0.13}\text{O}_2$ hollow nano/sub-microspheres samples calcinated at 800, 900, 950, and 1000 °C.

The influence of calcination temperature on the morphology has been investigated and presented in Figure 1, which shows

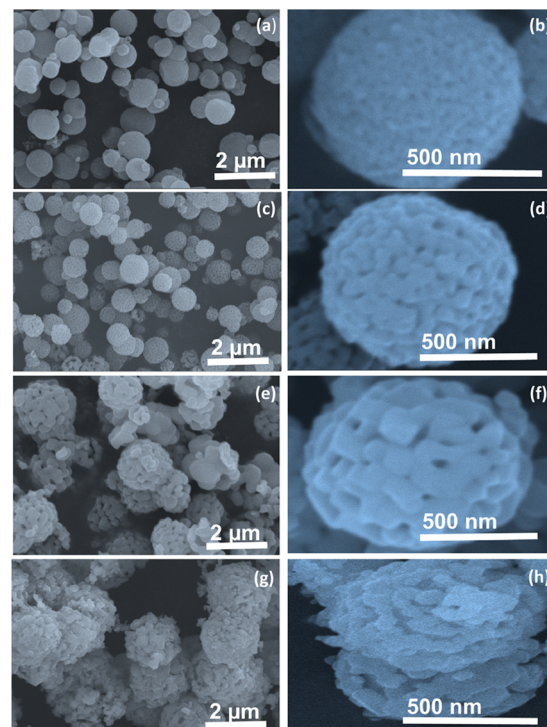


Figure 1. SEM images of LMNCO-800 (a, b), LMNCO-900 (c, d), LMNCO-950 (e, f), and LMNCO-1000 (g, h) hollow nano/sub-microspheres at low and high magnifications.

SEM images of LMNCO hollow nano/sub-microspheres (630–730 nm) formed by several 70–95 nm polyhedral smooth-edged primary nanoparticles. The primary LMNCO particle size gradually increases from 70 to 95 nm when the calcination temperature increases from 800 to 1000 °C, as shown in Table S1. However, there is no change in the morphology of secondary particles, but the primary particles are loosened on increasing the temperature. The SEM-energy-dispersive X-ray (EDX) elemental maps for LMNCO-950 samples were made to verify the distribution of the transition (Mn, Ni, Co, and O) metals and are shown in Figure S3c–f. The LMNCO-950 sample confirms the homogeneous distribution of the transition metal and reiterated in the SEM-EDX spectrum shown in Figure S3a. Each secondary particle analogous spherical morphology with a nano/sub-microspheres and we can observe porous on the surface of the secondary particles which are formed by the CO_2 escape during the MnCO_3 calcinations, the porosity can offer good

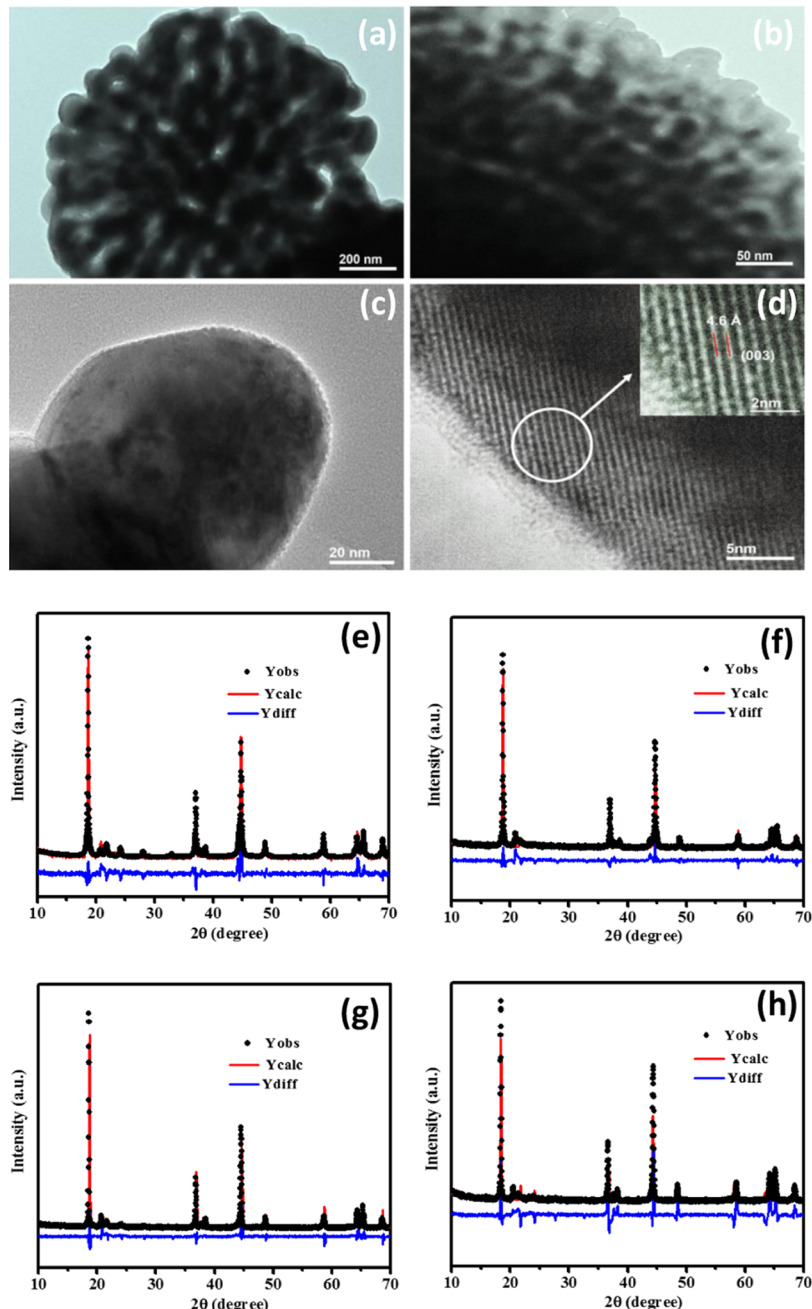


Figure 2. HR-TEM images of (a–d) LMNCO-950 hollow nano/sub-microspheres at low and high magnifications and Rietveld refinement results of X-ray diffraction (XRD) patterns of (e) LMNCO-800, (f) LMNCO-900, (g) LMNCO-950, and (h) LMNCO-1000 hollow nano/sub-microspheres.

electrolyte percolation. However, the LMNCO-1000 sample shows that the primary particles are more adhesive to other primary particles, which is not beneficial to the Li ion diffusion and electrolyte percolation.³³ Transmission electron microscopic (TEM) images of the LMNCO-950 sample are presented in Figure 2a–d. The spherical morphology with a hollow structure can be clearly observed, consistent with the SEM images. Figure 2c shows the typical bright-field high-resolution TEM (HR-TEM) image taken for the edge of a single primary nanoparticle, and the size is 84 nm. Figure 2d shows the edge of a single primary nanoparticle, demonstrating that the lattice distance of 4.6 Å agrees well with not only the {003} lattice spacing of the rhombohedral phase of LMO₂ (M

= Ni, Co, Mn) but also the (001) planes for monoclinic Li₂MnO₃.

The calcination temperature appears to significantly affect the surface area, pore volume, and pore size of the porous materials (Table S1). Figure S4a shows the N₂ adsorption/desorption isotherms of the as-prepared samples at different calcination temperatures, namely, LMNCO-800, LMNCO-900, LMNCO-950, and LMNCO-1000 hollow nano/sub-microspheres. All the samples show type IV isotherms with the H3-type hysteresis loop according to IUPAC classification, which is the characteristic of a mesoporous material. In addition, we observed a drastic reduction of surface area from 27.252 to 3.301 m² g⁻¹, when the calcination temperature of the LMNCO sample increased from 800 to 1000 °C. The

Table 1. Lattice Parameters and Crystal Sizes of the LMNCO-800, LMNCO-900, LMNCO-950, and LMNCO-1000 Hollow Nano/Sub-Microspheres

calcination samples	α (Å)	c (Å)	c/α	$I_{(003)}/I_{(104)}$ R	$I_{(006)} + I_{(102)}]/I_{(010)}$ R'	crystal size (nm)
LMNCO-800	2.8534	14.2405	4.9906	1.843	0.594	57.13
LMNCO-900	2.8508	14.2234	4.9893	1.784	0.7954	59.06
LMNCO-950	2.8527	14.2049	4.9794	1.441	0.624	62.04
LMNCO-1000	2.8473	14.2027	4.9881	2.039	0.494	68.76

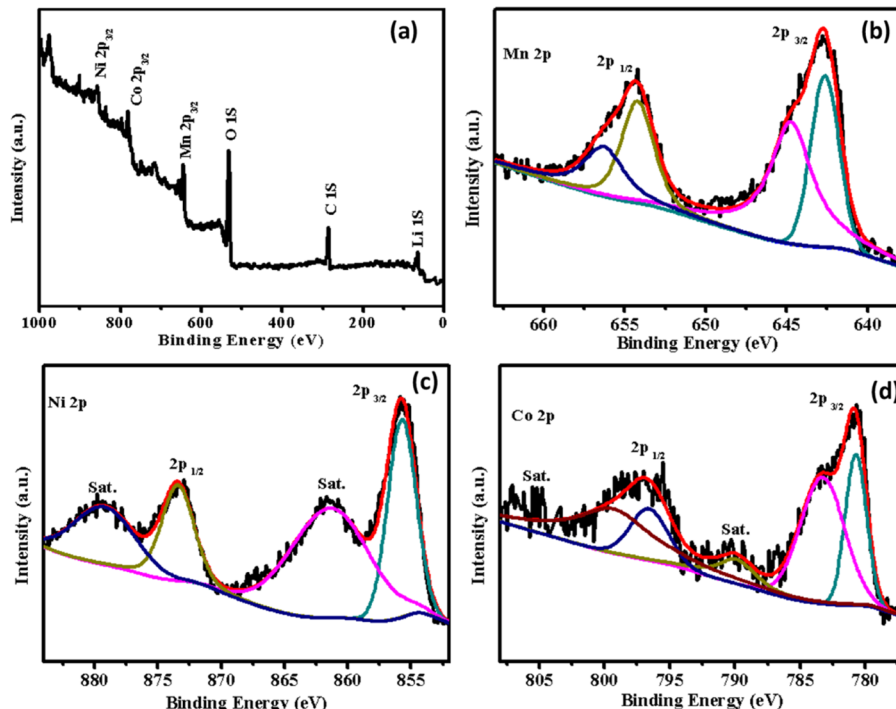


Figure 3. XPS spectra of LMNCO-950 hollow nano/sub-microspheres: (a) survey spectrum, (b) Mn 2p, (c) Ni 2p, (d) Co 2p.

subsequent decrease of pore volume (from 0.0315 to 0.0111 cm³ g⁻¹) and surface area upon thermal treatment at a higher temperature could be due to the increase of primary and secondary particle sizes of LMNCO samples. Indeed, the corresponding pore size distribution of LMNCO calcined materials was calculated by the Barrett–Joyner–Halenda method and plotted (Figure S4b), and materials exhibited an increase in the mesopore width from 11.392 to 40.743 nm due to the loosely bonded primary particles. The porous structure of LMNCO is also confirmed by SEM and TEM characterization, as shown in Figures 1a–h and 2a–d, respectively. These nano/micro mesoporous structures could effectively shorten the Li⁺ ion migration path, reduce the volume change during the charge–discharge cycling, and increase the contact area between the electrode and electrolyte, beneficial for the cycling performance.

The XRD pattern of the as-synthesized MnCO₃ nano/sub-microsphere precursor can be indexed to the pure rhombohedral phase of MnCO₃ (JCPDS card no. 44-1472),³⁴ and the spectra are presented in Figure S5a. The MnCO₃ microspheres decomposed into hollow MnO₂ by thermal treatment at 350 °C for 5 h. The XRD pattern shown in Figure S5b indicates the formation of a tetragonal phase of the MnO₂ hollow nano/sub-microspheres (JCPDS card no. 24-0735).³⁵ The LMNCO hollow nano/sub-microspheres are synthesized at various calcination temperatures, and their impact on the crystallinity and phase purity is shown in Figure S6, and the Rietveld

refinement fitting of the observed LMNCO peak, calculated peak, and their difference profile is presented in Figure 2e–h. The lattice parameters were calculated α-NaFeO₂ using XRD analysis software (TOPAS 4.1) shown in Table 1. All peaks are corresponding to a trigonal structure with the $R\bar{3}m$ space group. The $I_{(003)}/I_{(104)}$ ratio has been used as an indicator of cation mixing, that is, values higher than 1.2 indicate a high degree of cation mixing, due to the occupancy by other ions in the lithium interslab regions, and the reversible capacity of the cathode materials tends to decrease when the ratio is less than 1.2. In this work, the LMNCO-800 sample shows the highest $I_{(003)}/I_{(104)}$ ratio of 1.843, indicating that this sample has the lowest amount of cation mixing. However, as the calcination temperature increases to 950 °C, the ratio $I_{(003)}/I_{(104)}$ decreases dramatically, indicating that the LMNCO-950 sample has high degree of cation mixing. Further increase of calcination temperature to 1000 °C creates more Li/Mn cation mixing with enhanced crystallinity, which could be attributed to an increase of oxygen vacancies at high temperatures.^{21,36,37} Moreover, the diffraction peak in the 2θ range of 20–25° is for the alternate arrangement of Li⁺ and Mn⁴⁺ ions in the transition metal layers and the existence of a monoclinic crystal structure of Li₂MnO₃ (space group, $C2/m$).^{11,38,39}

The X-ray photoelectron spectroscopy (XPS) measurement was performed to gain more chemical insight into transition metal ions in the LMNCO-950 samples, and their corresponding spectra are shown in Figure 3. Initially, the binding energies

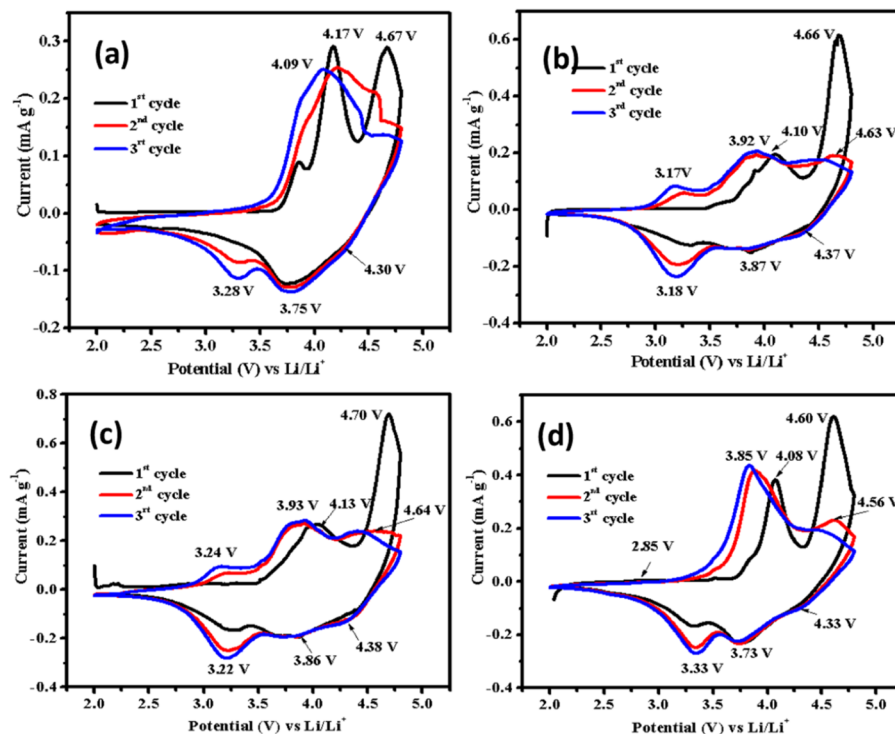


Figure 4. CV curves of initial three cycles: (a) LMNCO-800, (b) LMNCO-900, (c) LMNCO-950, and (d) LMNCO-1000 hollow nano/sub-microspheres at a scan rate of 0.1 mV s^{-1} .

are calibrated by referring the C 1s line to 284.6 eV. The XPS survey spectrum (Figure 3a) exhibits the existence of Li, Ni, Co, Mn, O, and C (reference specimen) without the presence of any impurities. Further, it can be clearly noted that there are four signals for both Ni 2p and Co 2p with two main peaks and two corresponding satellite peaks in the LMNCO-950 hollow nano/sub-microsphere samples using the Gaussian fitting method. However, the Mn 2p spectrum (Figure 3b) shows a pair of main spin-orbit lines at about 642.3 eV for Mn 2p_{3/2} and 654.2 eV for Mn 2p_{1/2}, with a separation of 11.5 eV, which indicates that the majority of Mn is in the Mn⁴⁺ state in LMNCO as in the case of previously published lithium-rich cathode materials.^{38–42} In detail, the Ni 2p XPS spectrum (Figure 3c) shows a sharp Ni 2p_{3/2} peak located at 855.2 eV and Ni 2p_{1/2} peak at about 873.1 eV with a separation of 17.9 eV, which are the characteristic peaks for the Ni²⁺cation. Further, two mild prominent peaks with binding energies of 858.2 and 876.5 eV are observed, indicating that the Ni ions are in a +2 oxidation state. Figure 3d shows the Co 2p spectrum, which reveals two major peaks at around 780.1 and 795.3 eV with a spin-orbit splitting of 15.2 eV, which can be ascribed to the Co 2p_{3/2} and Co 2p_{1/2} peaks, respectively, indicating the coexistence of Co²⁺. Two satellite peaks are detected at about 790.1 and 805.2 eV related to the fingerprint of Co³⁺ cations.^{38–42} Thus, it can be concluded that the well-formed LMNCO-950 cathode materials with hollow nano/sub-microspheres have been successfully prepared through our designed coprecipitation and chemical mixing method.

2.2. Electrochemical Properties. To evaluate the influence of calcination temperature on the electrochemical performance of LMNCO hollow nano/sub-microspheres, cyclic voltammograms (CVs) were performed at a scan rate of 0.1 mV s^{-1} between 2.0 and 4.8 V with 2032 coin-type cells shown in Figure 4. The Li- and Mn-rich LMNCO electrode

materials exhibit two main oxidation peaks in the first cycles at around 4.0–4.2 V corresponding to the reversible oxidation of Ni²⁺ to Ni⁴⁺ and Co³⁺ to Co⁴⁺ on extraction of Li⁺ ions from the LiMO₂ (M = Ni, Co) layered structure. On the other hand, the second oxidation peak appearing at around 4.6–4.7 V is due to the irreversible extraction of Li⁺ ions from the Li₂MnO₃ component, resulting in Li₂O formation through the oxygen activation.^{11,43} Furthermore, all of the LMNCO hollow nano/sub-microsphere samples show three distinguishable reduction peaks at around 4.3, 3.7, and 3.2 V. The first two peaks are ascribed to the reduction of Ni⁴⁺ and Co⁴⁺, while another peak at around 3.2 V is related to the Mn⁴⁺ reduction for balancing the charge of oxygen vacancies arising from the loss of oxygen during the first cycles. However, the sharp oxidation peak present in the first cycles appearing at around 4.6–4.7 V in all of the samples depletes in the second cycle due to the stabilization of the Li₂MnO₃ compounds. Meanwhile, the oxidation peak appearing at 4.08–4.17 V is shifted to the 3.8–4.08 V range; this is due to electrochemical polarization.⁴⁴ Significantly, the LMNCO-950 hollow nano/sub-microspheres show the irreversible oxidation peak at 4.7 V, which is relatively higher than the potential shows the other three LMNCO hollow nano/sub-microspheres electrodes is less even at the higher temperature calcined material, suggesting an improvement in the oxygen loss and decomposition of the electrolyte. Furthermore, the subsequent CV curves of the LMNCO-950 sample reveal better reversible and higher electrochemical properties due to the degree of symmetry associated with the shape of redox peaks. Thus, the sample LMNCO-950 possesses excellent structural stability and shows favorable cycle performances.

Galvanostatic charge/discharge performance of LMNCO hollow nano/sub-microspheres was examined between 2.0 and 4.8 V at 0.1 C (27 mA g^{-1}) for 50 cycles and is plotted in

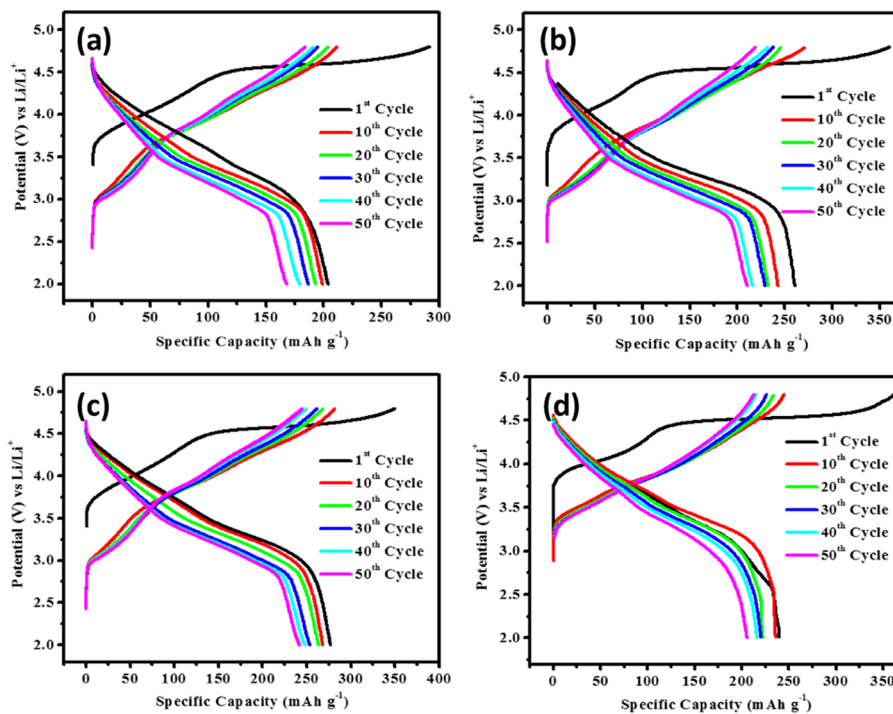


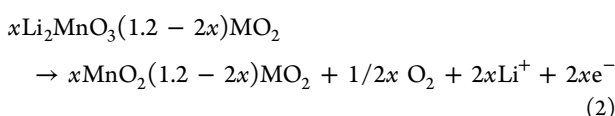
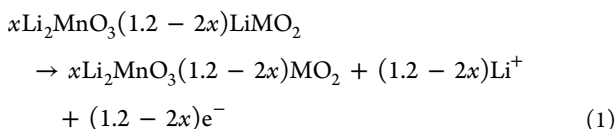
Figure 5. Charge/discharge curves of (a) LMNCO-800, (b) LMNCO-900, (c) LMNCO-950, and (d) LMNCO-1000 hollow nano/sub-microspheres at a 0.1C rate (27 mA g^{-1}).

Table 2. Comparison of Electrochemical Performance between Li-Rich Cathode Materials Reported in Previous Literatures and the As-Reported LMNCO-950 Cathode

samples name	discharge capacity (mAh g ⁻¹)				cycles/retention (%)				ref
	0.1C	1C	3C	5C	0.1	1C	3C	5C	
composite of $\text{Li}_{1.2}\text{Mn}_{0.54}\text{Ni}_{0.13}\text{Co}_{0.13}\text{O}_2$ -citric acid spheres-like $\text{Li}_{1.2}\text{Mn}_{0.54}\text{Ni}_{0.13}\text{Co}_{0.13}\text{O}_2$	263	215		188		200/61			9
$\text{LaNiO}_3 @ \text{Li}_{1.2}\text{Mn}_{0.54}\text{Ni}_{0.13}\text{Co}_{0.13}\text{O}_2$		255	172		50/93	300/81			11
hollow $\text{Li}_{1.2}\text{Mn}_{0.54}\text{Ni}_{0.13}\text{Co}_{0.13}\text{O}_2$ microspheres	285	161				50/92			12
$\text{Li}_{1.2}\text{Mn}_{0.54}\text{Ni}_{0.13}\text{Co}_{0.13}\text{O}_2$ nanofiber	220	138			50/93	100/81			35
$\text{Li}_{1.2}\text{Ni}_{0.2}\text{Mn}_{0.6}\text{O}_2$	219					100/80			13
$\text{Li}_{1.2}\text{Mn}_{0.54}\text{Ni}_{0.13}\text{Co}_{0.13}\text{O}_2$ hollow microspheres	259	196			25/93	50/95			45
Al_2O_3 coated $\text{Li}_{1.2}\text{Mn}_{0.54}\text{Ni}_{0.13}\text{Co}_{0.13}\text{O}_2$	287	234		150	100/85	100/81			46
LMNCO-950	282	210				90/97			47
	277	212	183	173	50/88	200/93	200/94	200/83	this work

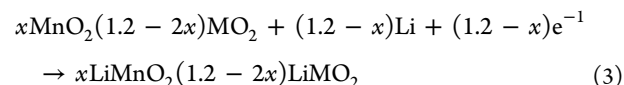
Figure 5. The first charging profiles were in good agreement with those of other reported Li- and Mn-rich LMNCO cathodes.^{9,11–13,45–47} All the samples exhibited two plateau regions in the first charging profiles: first plateau is up to 4.5 V, and the second plateau is between 4.5 and 4.8 V. It is generally accepted that $\text{Li}_{1.2}\text{Mn}_{0.54}\text{Co}_{0.13}\text{Ni}_{0.13}\text{O}_2$ electrodes are charged in two steps with different mechanisms during the initial charging process. This behavior can be explained as follows.

2.2.1. Charging Process.



As described in the reaction, the two plateau regions belong to $x\text{Li}_2\text{MnO}_3(1.2 - 2x)$ and LMO_2 , which is confirmed through the XRD results where the $\text{Li}_{1.2}\text{Mn}_{0.54}\text{Co}_{0.13}\text{Ni}_{0.13}\text{O}_2$ hollow nano/sub-microspheres are recognized as a mixture of trigonal ($R\bar{3}m$) and monoclinic ($C2/m$) structures.

2.2.2. Discharging Process.



The first chemical reaction, eq 1, explains the charging reaction where delithiation takes place below 4.5 V corresponding to the oxidation of Ni^{2+} to Ni^{4+} and Co^{3+} to Co^{4+} , and the second charging reaction, eq 2, occurs between 4.5 and 4.8 V, attributed to the irreversible oxygen loss from the Li_2MnO_3 component with the removal of Li_2O in the first irreversible charging process. During the discharge chemical reaction (eq 3), lithiation occurs at >3.0 V and the discharge plateau decreased sharply below 3.0 V, where the reduction of Ni^{4+} , Co^{4+} , and Mn^{4+} ions occurs and forms the original state

of the $\text{Li}_{1.2}\text{Mn}_{0.54}\text{Co}_{0.13}\text{Ni}_{0.13}\text{O}_2$ electrode material. The first cycle discharge capacity is higher than that from the next consequent cycles owing to the fact that the electrochemical behavior of the $\text{Li}_{1.2}\text{Mn}_{0.54}\text{Co}_{0.13}\text{Ni}_{0.13}\text{O}_2$ electrode is getting stabilized and it exercises non-electrochemical processes at ≤ 3.0 V; thus, lowered capacity retention than in the first cycles was observed. All the LMNCO electrode materials revealed the large irreversible capacity loss (Table S2) mainly due to the elimination of the oxygen ion vacancies and the lithium ion sites as well as side reactions with the electrolyte at the high operating voltage over 4.5 V.^{9,11–13,35,45–47} Interestingly, all the LMNCO electrode materials showed remarkably higher charge/discharge capacities than the other reported conventional cathode materials (e.g., LiCoO_2 , LiFePO_4 , and LiMn_2O_4)^{48–50} which is an important characteristic property of high-energy-density LMNCO hollow nano/sub-microsphere electrodes. The discharge capacity retention values of LMNCO-800, LMNCO-900, LMNCO-950, and LMNCO-1000 electrodes after 50 cycles were 81, 80, 87, and 85%, respectively, which are best among the previous reports, shown in Table 2. The Coulombic efficiencies have a great influence on the possible applications of Li- and Mn-rich layered cathode materials. Generally, the nanoparticle electrode shows a high surface area and increased electrode/electrolyte interface provokes the risk of severe side reactions including decomposition of electrolytes and consumption of lithium. In the present synthesized LMNCO secondary particles, the electrode/electrolyte contact surface area is higher, but the fouling and the dissolution of electrode were not found as inferred from the higher Coulombic efficiency. The specific solid–electrolyte interface (SEI) area can be reduced significantly with an electrolyte-blocking layer outside the assembled secondary particles, which can help to defer the side reactions between the electrolyte and the electrode and achieve excellent Coulombic efficiency.

To evaluate the high-rate capability of four LMNCO hollow nano/sub-microsphere electrodes, the fabricated cells were tested at various rates ranging from 0.2C (54 mA g^{-1}) to 10C (2700 mA g^{-1}). Figure 6a displays the measured discharge capacitance of LMNCO-800, LMNCO-900, LMNCO-950, and LMNCO-1000 hollow nano/sub-microspheres at different rate capabilities, and the corresponding charge/discharge curves of LMNCO hollow nano/sub-microspheres are presented in Figures 6b and S7a–c. The discharge capacities of the LMNCO-950 hollow nano/sub-microsphere electrodes were 229, 218, 211, 183, 173, 162, and 220 mAh g^{-1} at current rates of 0.2, 0.5, 1, 3, 5, 10, and 0.2C, respectively. Notably, the electrode could still deliver a capacity of more than 160 mAh g^{-1} even at 10C, equivalent to as high as 71% of discharge capacity at 0.2C. Additionally, the discharge capacity of LMNCO-950 is recovered to 220 mAh g^{-1} when the discharge rate was dropped back down to 0.2C, which is close to its initial discharge capacity under 0.2C rate. However, LMNCO-800, LMNCO-900, and LMNCO-1000 samples show less high-rate performance, where the discharge capacity at 10C rate dropped to 62, 65, and 62%, respectively, when compared with the discharge capacity of the same samples at 0.2C rate. The discharge capacities of all the LMNCO electrode materials slowly decreased when increasing the discharge rate. However, the LMNCO-950 hollow nano/sub-microsphere sample showed its superior electrochemical performance.

Figure 7a–d shows the electrochemical cycle performances of all the LMNCO hollow nano/sub-microsphere electrodes at

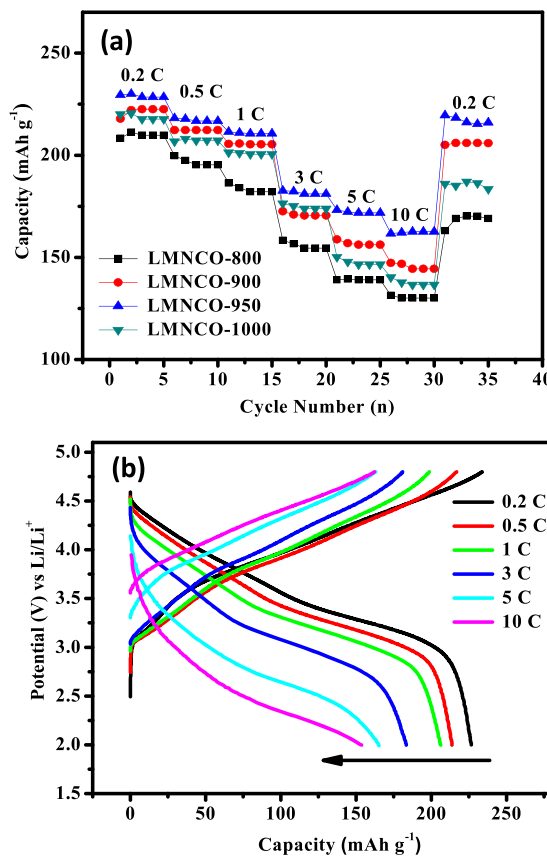


Figure 6. (a) Rate capability of LMNCO-800, LMNCO-900, LMNCO-950, and LMNCO-1000 hollow nano/sub-microspheres and (b) charge/discharge curves of LMNCO-950 at different C-rates.

1, 3, and 5C rates. The initial discharge capacities of 186, 158, and 139 mAh g^{-1} (LMNCO-800); 202, 176, and 157 mAh g^{-1} (LMNCO-900); 212, 183, and 173 mAh g^{-1} (LMNCO-950); and 201, 176, and 150 mAh g^{-1} (LMNCO-1000) with capacity retention values of 74, 70, and 55% (LMNCO-800); 89, 73, and 56% (LMNCO-900); 93, 94, and 83% (LMNCO-950); and 91, 90, and 85% (LMNCO-1000) after 200 cycles at 1, 3, and 5C, respectively, were obtained. All the LMNCO hollow nano/sub-microsphere samples show the average Columbic efficiency of 98%. It can be concluded that the LMNCO-950 hollow nano/sub-microsphere electrode sample exhibits the highest initial discharge capacity, good rate capability, and most stable cyclic performance, which may be benefitted from its excellent structural integrity. Meanwhile, the SEM and HR-TEM images of the LMNCO-950 electrode exhibit nanometer-sized primary particles and increased the pore size supports for the excellent electrochemical performance and the shorter diffusion distance of Li^+ ions helps in high-rate performance.

The electrochemical impedance spectrum (EIS) of all the LMNCO hollow nano/sub-microspheres electrodes is recorded at the 1st cycle and 200th cycle and is presented in Figure 8a,b. Each plot consists of a depressed semicircle in the high-frequency region and a straight line in the low-frequency range. The impedance spectra can be explained using an equivalent electric circuit shown in Figure S9, which consists of the electrolyte resistance (R_s), charge transfer resistance (R_{ct}), and Warburg impedance (Z_w). Table S3 shows the specific data of each resistance. As shown, the R_s and R_{ct} values increase during the subsequent cycles. Furthermore, after 200

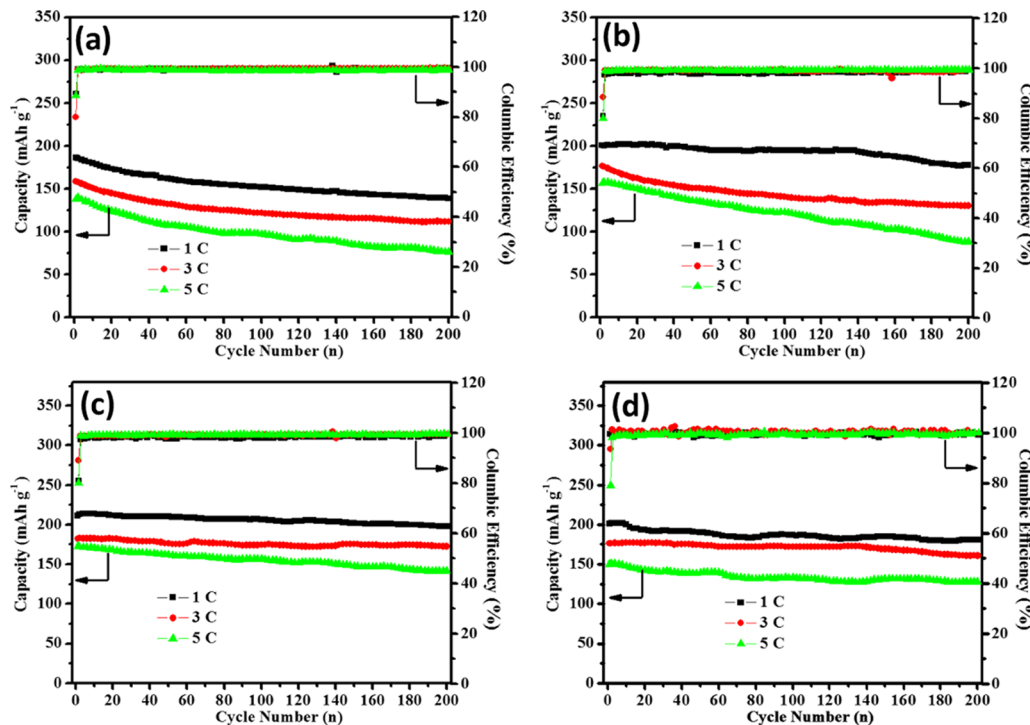


Figure 7. Cyclic stability and Coulombic efficiency of (a) LMNCO-800, (b) LMNCO-900, (c) LMNCO-950, and (d) LMNCO-1000 hollow nano/sub-microspheres for 200 cycles at 1, 3, and 5C rates.

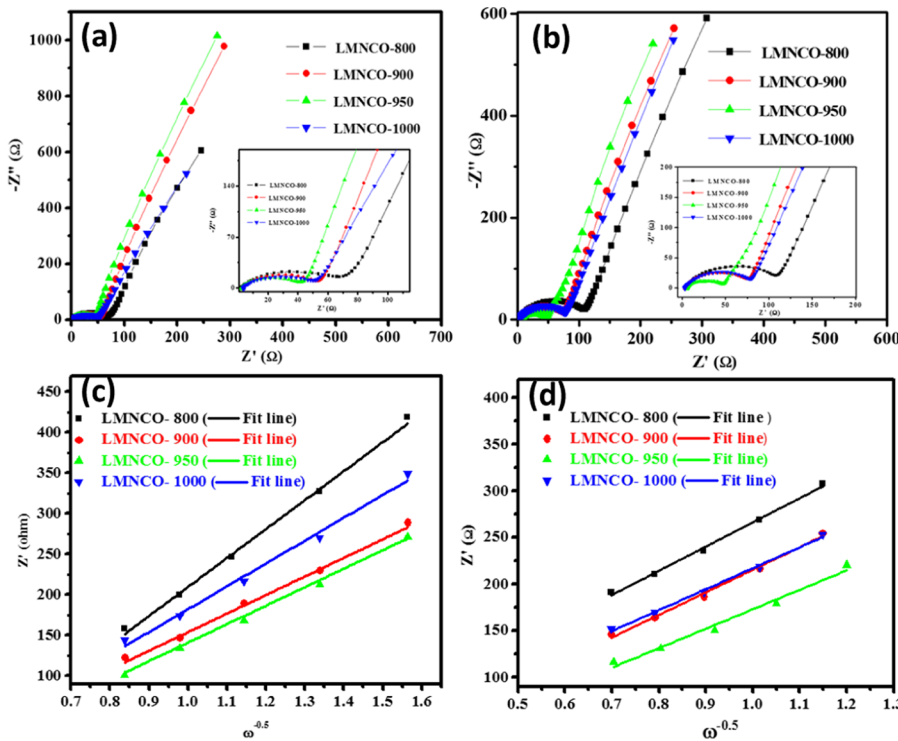


Figure 8. EIS data of the (a) initial cycles and (b) 200th cycle, and Z' vs $\omega^{-1/2}$ plots in the low-frequency region of (c) 1st cycle and (d) 200th cycle for LMNCO hollow nano/sub-microsphere electrodes.

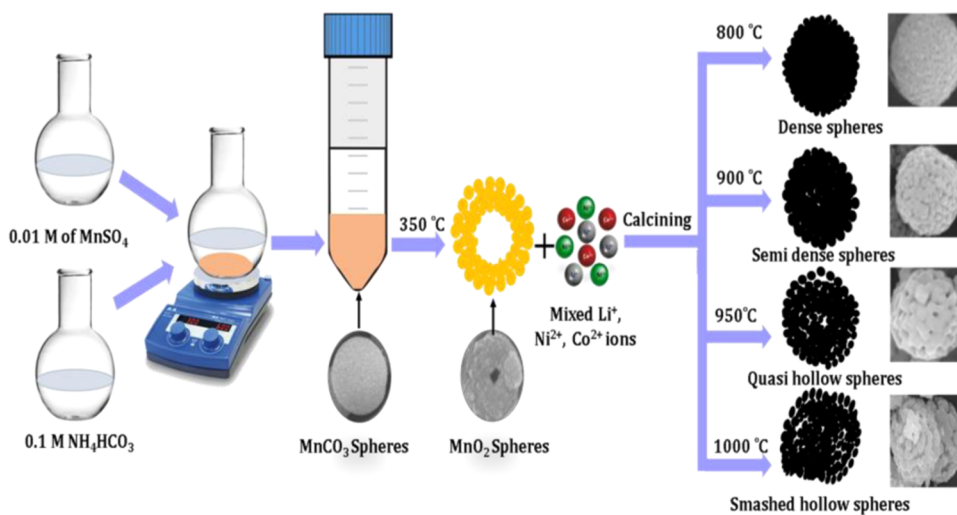
cycles, the increase of the R_s and R_{ct} values of LMNCO-950 is small, indicating that the SEI film formation on LMNCO-950 is negligible. The Li⁺ diffusion coefficient of the electrode has been calculated by the following equations, eqs 4 and 5.^{51,52}

$$D_{Li}^{+} = 0.5R^2T^2A^{-2}n^{-4}F^{-4}C^{-2}B^{-2} \quad (4)$$

$$Z_{re} = R_e + R_{ct} + \sigma\omega^{-1/2} \quad (5)$$

where R is the gas constant (8.314 J mol K), T is the absolute temperature (294 °C), A is the surface area of the cathode (1.3 cm²), n is the number of electrons per molecule during oxidation, F is the Faraday constant (96 485 C mol⁻¹), C is the

Scheme 1. Schematic Illustration of the Formation Process of the $\text{Li}_{1.2}\text{Mn}_{0.54}\text{Ni}_{0.13}\text{Co}_{0.13}\text{O}_2$ Hollow Nano/Sub-Microsphere Cathode Material



concentration of lithium ion, and B is the Warburg coefficient associated with the slope of linear fittings between Z' and the reciprocal square root of the angular frequency in the low-frequency region, as shown in Figure 8c,d. The calculated values of the lithium ion diffusion coefficient are listed in Table S3. The Li^+ diffusion coefficient of LMNCO-950 (200th cycle) is much higher than that of the other three samples, as shown in Figure 8d, while the LMNCO-950 electrode still presents the lowest values of R_s and R_{ct} and excellent Li-ion diffusion coefficient, indicating that the LMNCO-950 cathode still possesses relatively stable material interfaces even after long-term cycling performances without any disintegration.

To further understand the Li-ion storage performance in Li- and Mn-rich LMNCO-950 hollow nano/sub-microspheres, coin cells were initially activated with three cycles (2.0–4.8 V); after that, the cells were evaluated at different cutoff voltages (2.0–4.8, 2.0–4.7, 2.0–4.6, and 2.0–4.5 V) at 0.1C rate, and the discharge capacities were 273, 252, 227, and 201 mAh g^{-1} , respectively, in the first cycles (Figure S8a–d). The discharge capacity of LMNCO-950 decreased with decreasing cutoff voltage. However, the cyclic stability of the LMNCO-950 sample at different cutoff voltages was examined (4.5, 4.6, 4.7, and 4.8 V) at 1C rate for 200 cycles. The initial discharge capacities were obtained as 211, 205, 199, and 175 mAh g^{-1} at 4.8, 4.7, 4.6, and 4.5 V cutoff voltages at 1C rate, respectively; then, they gradually reduced on further cycling process. After 200 cycles, the capacity retention values were measured to be 93, 75, 83, and 89% for 4.8, 4.7, 4.6, and 4.5 V cutoff voltages, respectively (Figure S8e). On comparing all the cutoff voltage capacity retention after the 200th cycle, a higher capacity retention was observed for the 4.5 V cutoff voltage, which may be due to the excellent electroactive behavior of LMO_2 compounds. However, on increasing the cutoff voltage, the partial involvement of Li_2MnO_3 hinders the Li ion movements in the topotactical reactions, resulting in reduced capacity retention. In contrast to this, further, at a higher cutoff voltage of 4.8 V, Li_2MnO_3 and LMO_2 got involved in the host–guest process completely, resulting in a significantly improved performance of 197 mAh g^{-1} discharge capacity after the 200th cycle. Overall, the cyclic stability of prepared LMNCO-950 electrode materials coulomb efficiency is $\geq 98\%$ in all the cutoff voltages, due to the higher pore size, higher surface area

and nanoparticles are increased the electrode/electrolyte interaction. We have observed that our LMNCO-950 electrode materials have a higher cutoff voltage, superior rate capability, and excellent capacity retention than the commercially available cathodes.

To examine more detail the interfacial phenomenon of the LMNCO-950 electrode at different cutoff voltages, the EIS measurements were carried out after three charge–discharge cycles (Figure S9a,b), and the Nyquist plots showed that the cutoff voltages did not show any effect on the solution resistance (R_s). However, the charge transfer resistance (R_{ct}) significantly lowered for the cutoff voltage of 4.8 V (39.18 Ω) and 4.5 V (63.16 Ω), whereas it was higher for 4.6 V (76.99 Ω) and 4.7 V (79.67 Ω). The obtained R_s and R_{ct} and calculated D_{Li^+} values are summarized in Table S4. These results clearly indicate that the partially participating Li_2MnO_3 phase leads to a slower Li-ion intercalation/deintercalation process, which results in a reduced capacity retention at different cutoff voltages. In general, the capacity retention of all LMNCO electrodes at different cutoff voltages shows good electrochemical performances.

3. CONCLUSIONS

Li- and Mn-rich layered cathode materials, i.e., $\text{Li}_{1.2}\text{Mn}_{0.54}\text{Ni}_{0.13}\text{Co}_{0.13}\text{O}_2$, have been prepared at various calcination temperatures, and their structural and morphological properties and electrochemical performances at high cutoff voltages (2.0–4.8 V) have been systematically investigated. The results demonstrated that the electrochemical performance of the Li- and Mn-rich LMNCO cathode is optimized with respect to the calcination temperature and the primary particle size. An unsurpassed electrochemical performance of the LMNCO-950 electrode is achieved with an excellent discharge capacity of 277 mAh g^{-1} at 0.1C rate, and it is capable of delivering the capacity above 173 mAh g^{-1} at 5C rate and retention capacity of 82% of its initial capacity even after 200 cycles. On the other hand, increasing the calcination temperature (LMNCO-1000) leads to inferior long-term cycling stability and rate capability because of smashed quasi-hollow spheres and broken formation upon Li^+ deintercalation/intercalation that is closely related to the large primary nanoparticles in the electrode. These outcomes have high-

lighted the importance of optimizing the calcination temperature for preparing the Li- and Mn-rich hollow sphere electrodes. Besides, the optimization of calcination temperatures and primary and secondary particle sizes would depend on the compositions of the Li- and Mn-rich cathode materials; therefore, such parameters need to be carefully considered while tailoring the Li- and Mn-rich cathode materials to enhance their electrochemical performances. The Li- and Mn-rich LMNCO-950 electrode is an excellent alternate to the existing commercially available LMNC oxide cathode materials for high-energy lithium-ion batteries.

4. EXPERIMENTAL SECTION

4.1. Synthesis of LMNCO Hollow Nano/Sub-Microspheres. The target product ($\text{Li}_{1.2}\text{Mn}_{0.54}\text{Ni}_{0.13}\text{Co}_{0.13}\text{O}_2$) was synthesized using the coprecipitation approach as it has been widely used in the synthesis of hollow nano/sub-microspheres and is a cost-effective method. Scheme 1 is derived based on the synthesis process of $\text{Li}_{1.2}\text{Mn}_{0.54}\text{Ni}_{0.13}\text{Co}_{0.13}\text{O}_2$ hollow nano/sub-microspheres. Initially, the MnO_2 hollow nanosphere template was synthesized by the following process: 400 mL of 0.01 M MnSO_4 was taken in a 1000 mL round-bottom flask and 400 mL of 0.1 M ammonium bicarbonate was added slowly into the MnSO_4 solution. Stirring was continued for 2 h, and then, the MnCO_3 nanospheres were separated by centrifugation and washed with deionized water and ethanol to remove the impurities. The separated MnCO_3 nanospheres were dried at 120 °C for 12 h and decomposed at 350 °C for 5 h to obtain MnO_2 hollow nanospheres by elimination of CO_2 . The MnO_2 hollow nanospheres and the stoichiometric amount of $\text{Ni}(\text{NO}_3)_2 \cdot 6\text{H}_2\text{O}$, $\text{Co}(\text{NO}_3)_2 \cdot 6\text{H}_2\text{O}$, and $\text{LiOH} \cdot \text{H}_2\text{O}$ were dispersed in ethanol. The above added compounds were allowed to react with MnO_2 hollow nanospheres and evaporated at room temperature. To observe the influence of calcination temperature on the morphology and physicochemical and electrochemical properties of LMNCO hollow nano/sub-microspheres, the formed nanospheres were calcined at different temperatures: 800 °C (LMNCO-800), 900 °C (LMNCO-900), 950 °C (LMNCO-950), and 1000 °C (LMNCO-1000) for 10 h.

4.2. Structure and Morphological Characterization. The crystallinity and phase purity of the synthesized LMNCO hollow nano/sub-microsphere samples were characterized by powder X-ray diffraction (XRD, Bruker-D8 advance) using Cu K α radiation ($\lambda = 1.5406 \text{ \AA}$) at 40 kV/25 mA at a scan rate of 0.06° s $^{-1}$ with a 2 θ angle from 10 to 70. The morphology and particle size were examined by scanning electron microscopy (SEM, Hitachi SU8010) and high-resolution transmission electron microscopy (HR-TEM, Tecnai G2). Surface area, pore size, and pore volume of the synthesized LMNCO hollow nano/sub-microspheres were analyzed using the nitrogen adsorption-desorption isotherm method by a monosorb surface area analyzer (Quantachrome, Autosorb-6B). The XPS spectra were obtained using a PHI spectrometer (PerkinElmer, American) with monochromatic Mg radiation ($h\nu = 1253.6 \text{ eV}$) for LMNCO hollow nano/sub-microspheres.

4.3. Electrochemical Measurements. The electrochemical performances of the LMNCO hollow nano/sub-microsphere electrodes were tested in a CR2032 coin cell in half-cell LIB. The preparation of a positive electrode is as follows: 80 wt % active material, 10 wt % super P, and 10 wt % poly(vinylidene fluoride) were dissolved in *N*-methyl-2-pyrrolidone. The slurry was coated on the aluminum foil and

dried at 120 °C overnight in a vacuum oven. Then, the dried electrode sheet was cut into small disks of about 13 mm. The active material loading mass is $\sim 3.7 \text{ mg cm}^{-2}$. A lithium metal piece was used as a reference and counter electrode. A microporous polypropylene film was selected as a separator and soaked in the electrolytic solution of LiPF_6 in ethylene carbonate and dimethyl carbonate ($V_{\text{EC}}/V_{\text{DMC}} = 1:1$). Finally, the assembly of coin cell (CR2032) was made in an argon-filled glow box with H_2O and O_2 concentrations below 1 ppm. The galvanostatic charge–discharge tests were performed on the Autolab PGSTAT302N potentiostat instrument in a voltage range from 2.0 to 4.8 V. The electrochemical impedance spectroscopy (EIS) measurements were carried out on the Autolab PGSTAT-30 (Eco Chemie B.V., Netherlands) electrochemical workstation in the frequency range from 100 kHz to 0.01 Hz with the alternate current voltage amplitude of 5 mV.

■ ASSOCIATED CONTENT

Supporting Information

The Supporting Information is available free of charge at <https://pubs.acs.org/doi/10.1021/acsomega.9b02766>.

SEM images of MnCO_3 solid spheres and MnO_2 hollow spheres (Figure S1); TGA/DTA curves of MnO_2 with Li, Ni, Mn, Ni, and Co ions infused under an O_2 atmosphere at a heating rate of 5 °C min $^{-1}$ (Figure S2); elemental mapping of Mn, Ni, Co, and O (Figure S3); Brunauer–Emmett–Teller curves of LMNCO samples (Figure S4); XRD patterns of MnCO_3 and MnO_2 (Figure S5); XRD patterns of LMNCO samples (Figure S6); charge–discharge curves LMNCO samples at a high rate (Figure S7); charge–discharge curves of LMNCO-950 at different charging voltages (Figure S8); and EIS spectroscopy of the LMNCO-950 samples at different cutoff voltages (4.5, 4.6, 4.7, and 4.8 V) (Figure S9) (PDF)

■ AUTHOR INFORMATION

Corresponding Authors

*E-mail: apsakthivel@yahoo.com. Tel: +91 4565- 223 372. Fax: +91 4565- 225202, 22552 (S.P.).

*E-mail: cxyang@mail.mcut.edu.tw (C.-C.Y.).

ORCID

Shakkthivel Piraman: [0000-0003-4081-2823](http://orcid.org/0000-0003-4081-2823)

Notes

The authors declare no competing financial interest.

■ ACKNOWLEDGMENTS

The authors thank the Department of Science and Technology, Science and Engineering Research Board (EMR/2015/001475), New Delhi, India, for funding this project work. The authors also acknowledge the Battery Research Center of Green Energy, Ming Chi University of Technology, New Taipei City, Taiwan, for facilitating the electrochemical characterization at the Taiwan Education Exchange Program (TEEP@Asia plus) for the financial support.

■ REFERENCES

- (1) Li, H.; Ren, Y.; Yang, P.; Jian, Z.; Wang, W.; Xing, Y.; Zhang, S. Morphology and size controlled synthesis of the hierarchical

- structured $\text{Li}_{1.2}\text{Mn}_{0.54}\text{Co}_{0.13}\text{Ni}_{0.13}\text{O}_2$ cathode materials for lithium ion batteries. *Electrochim. Acta* **2019**, *297*, 406–416.
- (2) Di Lecce, D.; Verrelli, R.; Hassoun, J. Lithium-ion batteries for sustainable energy storage: recent advances towards new cell configurations. *Green Chem.* **2017**, *19*, 3442–3467.
- (3) Li, Y.; Yang, J.; Song, J. Design principles and energy system scale analysis technologies of new lithium-ion and aluminum-ion batteries for sustainable energy electric vehicles. *Renewable Sustainable Energy Rev.* **2017**, *71*, 645–651.
- (4) Shuai, H.; Li, J.; Hong, W.; Gao, X.; Zou, G.; Hu, J.; Hou, H.; Ji, X.; Liu, H. Electrochemically modulated $\text{LiNi}_{1/3}\text{Mn}_{1/3}\text{Co}_{1/3}\text{O}_2$ cathodes for lithium-ion batteries. *Small Methods* **2019**, *3*, No. 1900065.
- (5) Hu, L.; Freeland, J. W.; Cabana, J. Surface chemistry, passivation, and electrode performance in core-shell architectures of LiCoO_2 nanoplates. *ACS Appl. Energy Mater.* **2019**, *2*, 2149–2160.
- (6) Kumar, N.; Rodriguez, J. R.; Pol, V. G.; Sen, A. Facile synthesis of 2D graphene oxide sheet enveloping ultrafine 1D LiMn_2O_4 as interconnected framework to enhance cathodic property for li-ion battery. *Appl. Surf. Sci.* **2019**, *463*, 132–140.
- (7) Alagar, S.; Madhuvilakku, R.; Mariappan, R.; Piraman, S. Synthesize of Porous $\text{LiNi}_{0.5}\text{Mn}_{1.5}\text{O}_4$ microcubes for lithium-ion battery and supercapacitor applications. *J. Mater. Sci.: Mater. Electron.* **2018**, *29*, 1173–1181.
- (8) Zhang, J.; Hu, J.; Liu, Y.; Jing, Q.; Yang, C.; Chen, Y.; Wang, C. Sustainable and facile method for the selective recovery of lithium from cathode scrap of spent LiFePO_4 batteries. *ACS Sustainable Chem. Eng.* **2019**, *7*, 5626–5631.
- (9) Zheng, F.; Ou, X.; Pan, Q.; Xiong, X.; Yang, C.; Liu, M. The effect of composite organic acid (citric acid & tartaric acid) on microstructure and electrochemical properties of $\text{Li}_{1.2}\text{Mn}_{0.54}\text{Ni}_{0.13}\text{Co}_{0.13}\text{O}_2$ Li-rich layered oxides. *J. Power Sources* **2017**, *346*, 31–39.
- (10) Chen, C.; Geng, T.; Du, C.; Zuo, P.; Cheng, X.; Ma, Y.; Yin, G. Oxygen vacancies in SnO_2 surface coating to enhance the activation of layered li-rich $\text{Li}_{1.2}\text{Mn}_{0.54}\text{Ni}_{0.13}\text{Co}_{0.13}\text{O}_2$ cathode material for li-ion batteries. *J. Power Sources* **2016**, *331*, 91–99.
- (11) Huang, L.; Liu, L.; Wu, H.; Wang, Y.; Liu, H.; Zhang, Y. Optimization of synthesis parameters for uniform sphere-like $\text{Li}_{1.2}\text{Mn}_{0.54}\text{Ni}_{0.13}\text{Co}_{0.13}\text{O}_2$ as high performance cathode material for lithium ion batteries. *J. Alloys Compd.* **2019**, *775*, 921–930.
- (12) Zhang, X.; Hao, J.; Wu, L.; Guo, Z.; Ji, Z.; Luo, J.; Chen, C.; Shu, J.; Long, H.; Yang, F.; Volinsky, A. A. Enhanced electrochemical performance of perovskite LaNiO_3 coating on $\text{Li}_{1.2}\text{Mn}_{0.54}\text{Ni}_{0.13}\text{Co}_{0.13}\text{O}_2$ as cathode materials for li-ion batteries. *Electrochim. Acta* **2018**, *283*, 1203–1212.
- (13) Ma, D.; Zhang, P.; Li, Y.; Ren, X. $\text{Li}_{1.2}\text{Mn}_{0.54}\text{Ni}_{0.13}\text{Co}_{0.13}\text{O}_2$ -encapsulated carbon nanofiber network cathodes with improved stability and rate capability for li-ion batteries. *Sci. Rep.* **2015**, *5*, No. 1268.
- (14) Ming, L.; Zhang, B.; Cao, Y.; Zhang, J.-F.; Wang, C.-H.; Wang, X.-W.; Li, H. Effect of Nb and F co-doping on $\text{Li}_{1.2}\text{Mn}_{0.54}\text{Ni}_{0.13}\text{Co}_{0.13}\text{O}_2$ cathode material for high-performance lithium-ion batteries. *Front. Chem.* **2018**, *6*, 1–12.
- (15) Ma, Z.; Li, D.; Han, Y.; Shi, X.; Zhang, H.; Song, D.; Zhang, L. Li-rich layered/spinel cathode composite 3/4[$\text{Li}_2\text{MnO}_3 \cdot \text{LiC}_x\text{O}_2$]-1/4[LiC_xMn_4] ($\text{C}_x = \text{Cr-YCo}_y$) for li-ion batteries. *J. Electrochem. Soc.* **2019**, *166*, A5065–A5074.
- (16) Zhou, Y.; Wang, Y.; Li, S.; Mei, J.; Liu, H.; Liu, H.; Liu, G. Irregular micro-sized $\text{Li}_{1.2}\text{Mn}_{0.54}\text{Ni}_{0.13}\text{Co}_{0.13}\text{O}_2$ particles as cathode material with a high volumetric capacity for li-ion batteries. *J. Alloys Compd.* **2017**, *695*, 2951–2958.
- (17) Wu, F.; Wang, H.; Bai, Y.; Li, Y.; Wu, C.; Chen, G.; Liu, L.; Ni, Q.; Wang, X.; Zhou, J. Hierarchical microspheres and nanoscale particles: effects of morphology on electrochemical performance of $\text{Li}_{1.2}\text{Mn}_{0.54}\text{Ni}_{0.13}\text{Co}_{0.13}\text{O}_2$ cathode material for lithium-ion batteries. *Solid State Ionics* **2017**, *300*, 149–156.
- (18) Wu, F.; Tian, J.; Su, Y.; Wang, J.; Zhang, C.; Bao, L.; He, T.; Li, J.; Chen, S. Effect of Ni^{2+} content on lithium/nickel disorder for Ni-rich cathode materials. *ACS Appl. Mater. Interfaces* **2015**, *7*, 7702–7708.
- (19) Chen, L.; Chen, Z.; Liu, S.; Zhang, H.; Huang, Q. Study on highly compacted LiFePO_4/C cathode materials for high-performance 18650 Li-Ion Batteries. *Int. J. Electrochem. Sci.* **2018**, *13*, 5413–5424.
- (20) Okubo, M.; Hosono, E.; Kim, J.; Enomoto, M.; Kojima, N.; Kudo, T.; Zhou, H.; Honma, I. Nanosize effect on high-rate li-ion intercalation in LiCoO_2 electrode. *J. Am. Chem. Soc.* **2007**, *129*, 7444–7452.
- (21) Zheng, J.; Yan, P.; Estevez, L.; Wang, C.; Zhang, J. G. Effect of calcination temperature on the electrochemical properties of nickel-rich $\text{LiNi}_{0.76}\text{Mn}_{0.14}\text{Co}_{0.10}\text{O}_2$ cathodes for lithium-ion batteries. *Nano Energy* **2018**, *49*, 538–548.
- (22) Zheng, J.; Xiao, J.; Zhang, J. G. The roles of oxygen non-stoichiometry on the electrochemical properties of oxide-based cathode materials. *Nano Today* **2016**, *11*, 678–694.
- (23) Bi, Y.; Yang, W.; Du, R.; Zhou, J.; Liu, M.; Liu, Y.; Wang, D. Correlation of oxygen non-stoichiometry to the instabilities and electrochemical performance of $\text{LiNi}_{0.8}\text{Co}_{0.1}\text{Mn}_{0.1}\text{O}_2$ utilized in lithium ion battery. *J. Power Sources* **2015**, *283*, 211–218.
- (24) Nayak, P. K.; Yang, L.; Pollok, K.; Langenhorst, F.; Aurbach, D.; Adelhelm, P. Investigation of $\text{Li}_{1.17}\text{Ni}_{0.20}\text{Mn}_{0.53}\text{Co}_{0.10}\text{O}_2$ as an Interesting Li and Mn-rich oxide cathode materials by electrochemical means, microscopy and in situ electrochemical dilatometry. *ChemElectroChem* **2019**, *1*–27.
- (25) Chang-Jian, C. W.; Cho, E. C.; Huang, J. H.; Huang, J. H.; Chou, J. A.; Ho, B. C.; Lee, K. C.; Hsiao, Y. S. Spray-drying synthesis of $\text{Li}_4\text{Ti}_5\text{O}_{12}$ microspheres in pilot scale using TiO_2 Nanosheets as starting materials and their application in high-rate lithium ion battery. *J. Alloys Compd.* **2019**, *773*, 376–386.
- (26) He, Z.; Wang, Z.; Chen, H.; Huang, Z.; Li, X.; Guo, H.; Wang, R. Electrochemical performance of zirconium doped lithium rich layered $\text{Li}_{1.2}\text{Mn}_{0.54}\text{Ni}_{0.13}\text{Co}_{0.13}\text{O}_2$ oxide with porous hollow structure. *J. Power Sources* **2015**, *299*, 334–341.
- (27) Lou, M.; Zhong, H.; Yu, H. T.; Fan, S. S.; Xie, Y.; Yi, T. F. $\text{Li}_{1.2}\text{Mn}_{0.54}\text{Ni}_{0.13}\text{Co}_{0.13}\text{O}_2$ hollow hierarchical microspheres with enhanced electrochemical performances as cathode material for lithium-ion battery application. *Electrochim. Acta* **2017**, *237*, 217–226.
- (28) Li, Y.; Mei, J.; Guo, X.; Zhong, B.; Liu, H.; Liu, G.; Dou, S. Hollow $\text{Li}_{1.2}\text{Mn}_{0.54}\text{Ni}_{0.13}\text{Co}_{0.13}\text{O}_2$ micro-spheres synthesized by a co-precipitation method as a high-performance cathode material for li-ion batteries. *RSC Adv.* **2016**, *6*, 70091–70098.
- (29) Xie, Q.; Zeng, D.; Ma, Y.; Lin, L.; Wang, L.; Peng, D. L. Synthesis of $\text{ZnO-ZnCo}_2\text{O}_4$ hybrid hollow microspheres with excellent lithium storage properties. *Electrochim. Acta* **2015**, *169*, 283–290.
- (30) Xie, Q.; Zhang, X.; Wu, X.; Wu, H.; Liu, X.; Yue, G.; Yang, Y.; Peng, D. Electrochimica acta yolk-shell ZnO-C microspheres with enhanced electrochemical performance as anode material for lithium ion batteries. *Electrochim. Acta* **2014**, *125*, 659–665.
- (31) Fu, F.; Tang, J.; Yao, Y.; Shao, M. Hollow Porous Hierarchical-Structured $0.5\text{Li}_2\text{MnO}_3 \cdot 0.5\text{LiMn}_{0.4}\text{Co}_{0.3}\text{Ni}_{0.3}\text{O}_2$ as a high-performance cathode material for lithium-ion batteries. *ACS Appl. Mater. Interfaces* **2016**, *8*, 25654–25659.
- (32) Xie, Q.; Ma, Y.; Wang, X.; Zeng, D.; Wang, L.; Mai, L.; Peng, D. L. Electrostatic assembly of sandwich-like Ag-C@ZnO-C@Ag-C hybrid hollow microspheres with excellent high-rate lithium storage properties. *ACS Nano* **2016**, *10*, 1283–1291.
- (33) Zhao, T.; Zhou, N.; Zhang, X.; Xue, Q.; Wang, Y.; Yang, M.; Li, L.; Chen, R. Structure evolution from layered to spinel during synthetic control and cycling process of fe-containing li-rich cathode materials for lithium-ion batteries. *ACS Omega* **2017**, *2*, 5601–5610.
- (34) Yao, Y.; Liu, H.; Li, G.; Peng, H.; Chen, K. Multi-shelled porous $\text{LiNi}_{0.5}\text{Mn}_{1.5}\text{O}_4$ microspheres as a 5 v cathode material for lithium-ion batteries. *Mater. Chem. Phys.* **2014**, *143*, 867–872.
- (35) Duraisamy, S.; Penki, T. R.; Kishore, B.; et al. Porous, hollow $\text{Li}_{1.2}\text{Mn}_{0.53}\text{Ni}_{0.13}\text{Co}_{0.13}\text{O}_2$ microspheres as a positive electrode material for Li-Ion Batteries. *J. Solid State Electrochem.* **2017**, *21*, 437–445.

- (36) Zhao, E.; Li, Q.; Meng, F.; Liu, J.; Wang, J.; He, L.; Jiang, Z.; Zhang, Q.; Yu, X.; Gu, L.; Yang, W.; Li, H.; Wang, F.; Huang, X. Stabilizing oxygen lattice and reversible oxygen redox chemistry through structural dimensionality in lithium-rich cathode oxides. *Angew. Chem., Int. Ed.* **2019**, *58*, 4323–4327.
- (37) Liu, P.; Zhang, H.; He, W.; Xiong, T.; Cheng, Y.; Xie, Q.; Ma, Y.; Zheng, H.; Wang, L.; Zhu, Z.-Z.; Peng, Y.; Mai, L.; Peng, D.-L. Lithium deficiencies engineering in li-rich layered oxide $\text{Li}_{1.098}\text{Mn}_{0.533}\text{Ni}_{0.113}\text{Co}_{0.138}\text{O}_2$ for high-stability cathode. *J. Am. Chem. Soc.* **2019**, *141*, 10876–10882.
- (38) Tian, Y.; Chen, M.; Xue, S.; Cai, Y.; Huang, Q.; Liu, X.; Li, W. Template-determined microstructure and electrochemical performances of li-rich layered metal oxide cathode. *J. Power Sources* **2018**, *401*, 343–353.
- (39) Sun, K.; Peng, C.; Li, Z.; Xiao, Q.; Lei, G.; Xiao, Q.; Ding, Y.; Hu, Z. Hybrid LiV_3O_8 /carbon encapsulated $\text{Li}_{1.2}\text{Mn}_{0.54}\text{Ni}_{0.13}\text{Co}_{0.13}\text{O}_2$ with improved electrochemical properties for lithium ion batteries. *RSC Adv.* **2016**, *6*, 28729–28736.
- (40) Co, L.; Mn, O.; Zro, L.; Liang, H.; Wang, Z.; Guo, H.; Wang, J.; Leng, J. Applied surface science improvement in the electrochemical performance of $\text{LiNi}_{0.8}\text{Co}_{0.1}\text{Mn}_{0.1}\text{O}_2$ cathode material by Li_2ZrO_3 coating. *Appl. Surf. Sci.* **2017**, *423*, 1045–1053.
- (41) Chong, S.; Chen, Y.; Yan, W.; Guo, S.; Tan, Q.; Wu, Y.; Jiang, T.; Liu, Y. Suppressing capacity fading and voltage decay of li-rich layered cathode material by a surface nano-protective layer of CoF_2 for lithium-ion batteries. *J. Power Sources* **2016**, *332*, 230–239.
- (42) Zhao, Y.; Xia, M.; Hu, X.; Zhao, Z.; Wang, Y.; Lv, Z. Effects of Sn doping on the structural and electrochemical properties of $\text{Li}_{1.2}\text{Ni}_{0.2}\text{Mn}_{0.8}\text{O}_2$ Li-rich cathode materials. *Electrochim. Acta* **2015**, *174*, 1167–1174.
- (43) Ma, D.; Li, Y.; Zhang, P.; Cooper, A. J.; Abdelkader, A. M.; Ren, X.; Deng, L. Mesoporous $\text{Li}_{1.2}\text{Mn}_{0.54}\text{Ni}_{0.13}\text{Co}_{0.13}\text{O}_2$ nanotubes for high-performance cathodes in li-ion batteries. *J. Power Sources* **2016**, *311*, 35–41.
- (44) Li, N.; He, Y. S.; Wang, X.; Zhang, W.; Ma, Z. F.; Zhang, D. Incorporation of rubidium cations into $\text{Li}_{1.2}\text{Mn}_{0.54}\text{Co}_{0.13}\text{Ni}_{0.13}\text{O}_2$ layered oxide cathodes for improved cycling stability. *Electrochim. Acta* **2017**, *231*, 363–370.
- (45) Li, L.; Wang, L.; Zhang, X.; Xue, Q.; Wei, L.; Wu, F.; Chen, R. 3D reticular $\text{Li}_{1.2}\text{Ni}_{0.2}\text{Mn}_{0.6}\text{O}_2$ cathode material for lithium-ion batteries. *ACS Appl. Mater. Interfaces* **2017**, *9*, 1516–1523.
- (46) Li, H.; Wei, X.; Yang, P.; Ren, Y.; Wang, S.; Xing, Y.; Zhang, S. Uniform $\text{Li}_{1.2}\text{Mn}_{0.54}\text{Ni}_{0.13}\text{Co}_{0.13}\text{O}_2$ hollow microspheres with improved electrochemical performance by a facile solvothermal method for lithium ion batteries. *Electrochim. Acta* **2018**, *261*, 86–95.
- (47) Chen, Y.; Wang, X.; Zhang, J.; Chen, B.; Xu, J.; Zhang, S.; Zhang, L. Al_2O_3 -coated $\text{Li}_{1.2}\text{Mn}_{0.54}\text{Ni}_{0.13}\text{Co}_{0.13}\text{O}_2$ nanotubes as cathode materials for high-performance lithium-ion batteries. *RSC Adv.* **2019**, *9*, 2172–2179.
- (48) Li, S.; Zhu, K.; Liu, J.; Zhao, D.; Cui, X. Porous LiMn_2O_4 microspheres with different pore size: preparation and application as cathode materials for lithium ion batteries. *J. Electrochem. Energy Convers. Storage* **2018**, *16*, 011006-1–011006-8.
- (49) Fischer, M. G.; Hua, X.; Wilts, B. D.; Castillo-Martínez, E.; Steiner, U. Polymer-templated LiFePO_4/C nanonetworks as high-performance cathode materials for lithium-ion batteries. *ACS Appl. Mater. Interfaces* **2018**, *10*, 1646–1653.
- (50) Wang, L.; Ma, J.; Wang, C.; Yu, X.; Liu, R.; Jiang, F.; Sun, X.; Du, A.; Zhou, X.; Cui, G. A Novel bifunctional self-stabilized strategy enabling 4.6 V LiCoO_2 with excellent long-term cyclability and high-rate capability. *Adv. Sci.* **2019**, *6*, No. 1900355.
- (51) Yang, C.; Ou, X.; Xiong, X.; Zheng, F.; Hu, R.; Chen, Y.; Liu, M.; Huang, K. V_5S_8 -Graphite hybrid nanosheets as a high rate-capacity and stable anode material for sodium-ion batteries. *Energy Environ. Sci.* **2017**, *10*, 107–113.
- (52) Zheng, F.; Ou, X.; Pan, Q.; Xiong, X.; Yang, C.; Fu, Z.; Liu, M. Nanoscale gadolinium doped ceria (GDC) surface modification of li-rich layered oxide as a high performance cathode material for lithium ion batteries. *Chem. Eng. J.* **2018**, *334*, 497–507.